ORIGINAL ARTICLE

An elastoplastic model for gas flow characteristics around drainage borehole considering post-peak failure and elastic compaction

Yi Xue[1,2] · Faning Dang[1,2] · Fengyin Liu[1,2] · Rongjian Li[1,2] · P. G. Ranjith[3] · Songhe Wang[1,2] · Zhengzheng Cao[4] · Yugui Yang[4]

Abstract

The excavation and drainage drilling for underground mining induces stress redistribution around the gas drainage borehole, thus forming three physical zones: residual state zone, strain softening zone and elastic zone. The formation process of these zones contains complex interactions among deformation, natural gas flow, and coal seam damage. A better understanding of these interactions could provide better guidance for the gas drainage engineering. Extensive studies have focused on the effect of effective stress or effective strain on permeability variation based on the poroelastic theory. Meanwhile, as there is few permeability models taking the post-peak failure effect into account, previous permeability variation analysis seldom commonly considered the elastoplastic characteristic of coal seam, which results in the permeability misestimation. Therefore, this study proposes a new approach to analyze this interaction process. The innovation of this approach is that it takes into account the influence of coal permeability enhancement in failure zone and the volumetric compaction in elastic zone around the drainage borehole. In this approach, analytical solutions of stress and strain are developed to include both the strain softening around a gas drainage borehole and the compaction in elastic zone. These solutions thus remove the flaws that previous studies did not consider the compaction in elastic zone. Further, a new permeability model is proposed by the introduction of damage enhancement coefficient for post-peak failure. Third, the permeability distribution of coal around a gas drainage borehole is calculated based on the analytical solutions and the new permeability model. Fourth, the gas flow equation is numerically solved to obtain gas pressure profiles. The gas content computed by this approach is verified by field data. Finally, parametric study is carried out to investigate the effect of the damage enhancement coefficient, initial geo-stress, drilling volume, and uniaxial strength on the gas pressure and the permeability around the gas drainage borehole. Based on these numerical analyses, it is found that the evolution of permeability is closely related to the physical properties of coal and the geological condition of coal seam. Higher initial geo-stress and lower failure strength have larger unloading zone and higher permeability enhancement. This compaction helps the coal seam form a flow-shielding zone near the interface between plastic zone and elastic zone. The gas flow in the coal around the drainage borehole can be divided into four different zones.

Keywords Permeability distribution · Pressure profile · Post-peak failure · Rock compaction · Damage enhanced coefficient

✉ Yi Xue
xueyi@xaut.edu.cn

1 State Key Laboratory of Eco-hydraulics in Northwest Arid Region, Xi'an University of Technology, Xi'an 710048, China

2 Institute of Geotechnical Engineering, Shaanxi Provincial Key Laboratory of Loess Mechanics and Engineering, Xi'an University of Technology, Xi'an 710048, China

3 Deep Earth Energy Laboratory, Department of Civil Engineering, Monash University, Building 60, Melbourne, VIC 3800, Australia

4 State Key Laboratory for Geomechanics and Deep Underground Engineering, China University of Mining and Technology, Xuzhou 221116, China

List of symbols

R_0, R_b, R_p	Radii of the borehole, residual state zone and strain softening zone (m)
$\sigma_\theta^p, \sigma_r^p$	Hoop and radial stress components in the strain-softening zone (MPa)
m_e, m_p, m_b	Dilatation coefficients in the elastic zone, the strain-softening zone and the residual state zone (–)
σ_c^*	Uniaxial residual strength (MPa)
σ_{R_p}	Stress on the boundary between the strain-softening zone and the elastic zone (MPa)
$\Delta\varepsilon_\theta$	Increments of hoop strain (–)
E	Young's modulus of coal (MPa)
p_i	Initial geo-stress (MPa)
α	Biot coefficient (–)
b	Fracture aperture (m)
τ	Tortuosity parameter (–)
γ	Mutation coefficient (–)
λ	Damage enhancement coefficient (–)
$\vec{q}_g$	Velocity (m/s)
v^b	Volumetric strain in the residual state zone (–)
p	Gas pressure (MPa)
Q_m	Gas source by injection (m³/s)
ρ_{ga}	Gas density at standard conditions (kg/m³)
ρ_c	Density of coal (kg/m³)
V_{sg}	Content of absorbed gas
K	Bulk modulus of coal (MPa)
k_g	Permeability of coal (m²)
ϕ_0	Initial porosity (–)
k_0	Initial permeability (m²)
$\sigma_\theta^e, \sigma_r^e$	Hoop and radial stress components in the elastic zone (MPa)
$\sigma_\theta^b, \sigma_r^b$	Hoop and radial stress components in the residual state zone (MPa)
v^e, v^p, v^b	Volumetric strain in elastic zone, the strain-softening zone and the residual state zone (–)
σ_c^p	Uniaxial compressive strength (MPa)
R_p	Boundary between the strain-softening zone and the elastic zone (m)
$\Delta\varepsilon_r$	Increments of radial strain (–)
p_s	Supporting traction of cavity (MPa)
k_s	Softening coefficient of coal (–)
K_p	Modulus of pores (MPa)
l_n	Sum of the lengths of the multi-fractures (m)
Δp	Pressure difference (MPa)
c_f	Compression coefficient of fracture (MPa⁻¹)
σ_e	Effective stress (MPa)
V_L	Adsorption capacity of coal (m³/kg)
P_L	Langmuir pressure constant (MPa)
ε_s	Sorption-induced volumetric strain (–)
m	Mass content (kg/m³)
ρ_g	Density of CH_4 at standard condition (kg/m³)
p_0	Initial gas pressure (MPa)
K_s	Bulk modulus of coal grains (MPa)
t	Time (s)
ϕ	Coal porosity (–)
μ	Gas dynamic viscosity (Pa s)
φ	Internal friction angle of coal (°)

Introduction

The control of gas-induced disaster is still a heavy task in mining industry. With the increase of mining depth, coal mine accidents such as gas-induced disaster still occur frequently although some measures such as mining automation have been made. Different engineering measures (Alonso et al. 2003; Karacan 2007; Liu et al. 2017) have been employed to reduce the gas content near the excavation. These measures can reduce gas accumulation and suppress gas outbursts to some extent, thus avoiding most of gas-induced accidents. It is shown that underground excavation and coalbed methane (CBM) drilling may cause unloading failure of coal seam and increase the emissions of coal seam gas (Yin et al. 2015). Therefore, understanding the accumulation of methane near the coal wall along the borehole is meaningful for the safety evaluation in coal mining industry.

The accumulation of methane near the coal wall along the wellbore is the result of the interaction of rock deformation and gas flow. In rock deformation process, some analytical solutions are available for both stress and displacement. They used different constitutive models such as an elastic–plasticity model after the combination of failure criterion (Carranza-Torres 2004; Guan et al. 2007; Yang and Huang 2010; Zhang et al. 2010; Lu and Yang 2013). For examples, Brown et al. (1983) presented a closed-form solution and an analytical solution for a plastic model by means of a stepwise sequence of calculations. They also proposed a damage variable to take the degradation of materials or the degree of strain softening into accounts. All of these studies ignored the volumetric strain or compaction in the pre-peak deformation stage. When compaction is ignored in this pre-peak deformation stage, it may cause a big error in calculating stress and strain around the borehole. Because coal experiences shear compaction in this pre-peak deformation process, the compaction may affect the distribution of permeability and the accumulation of natural gas near the borehole. Therefore, the compaction in the elastic zone has to be carefully considered when the accumulation of natural gas or permeability distribution around the borehole is computed.

Coal is a typical pore/fracture system (Gilman and Beckie 2000; Clarkson et al. 2007; Booth et al. 2017; Salmachi and Karacan 2017). Coal permeability is due

to a set of fractures known as cleats, it is stress and desorption dependent. Coal permeability enhancement due to stress and desorption can be measured by analysis of production data (Salmachi and Yarmohammadtooski 2015). Although coal permeability models have been studied extensively (Cui and Bustin 2005; Palmer and Mansoori 1996; Qu et al. 2014; Salmachi et al. 2016; Shi and Durucan 2004; Li et al. 2017), a fewer publications are available to account for the permeability behaviors of coals at the post-peak unloading failure stage. Chen et al. (2013) measured the permeability of reconstituted coal specimens and investigated the relationship between damage and coal permeability through the observation of coal microstructures by CT scanning. Wang et al. (2013) conducted post-peak permeability experiments to study the coal permeability under different stress and pore pressure. These experiments revealed the influence of fracture on the permeability of coal. Besides the experimental studies, some researchers tried to establish an effective coal permeability model which is applicable in post-failure state. For example, Xue et al. (2017) adopted an exponential relationship between permeability and volumetric strain to calculate the post-failure permeability. Chen et al. (2016) proposed a post-peak permeability model through adding the logistic growth function and a correction factor to the computational formula of the pre-peak permeability. These models were established by fitting the parameters with the experimental data and the parameters in these functions do not have actual physical meaning, thus it cannot essentially reveal the permeability evolution characteristics of coal mass in the post-peak stage. Tang et al. (2002) and Men et al. (2014) analyzed the flow, stress and damage at the post-peak unloading stage by means of brittle–elastic material with residual strength. In their model, the damage is the main factor that causes the growth of fracture and permeability in the post-peak stage. The permeability increases dramatically at the failure of the elements and a permeability jump is given to these elements with sudden damage although the permeability jump is inconsistent with the experimental observation. Based on the work of Tang et al. (2002), Zhu et al. (2016) proposed a new post-peak permeability model, and permeability increased continuously with the growth of damage of coal. Both of these two theoretical models are established based on a clear physical meaning that the increase in permeability is induced by damage. However, because the value of the parameter in these models is obtained based on experience, there may be the deviations between the results of these models and the experimental results. These studies on permeability models in the post-peak unloading stage were meaningful, but the complex seepage mechanism in post-peak stage is still not clear. Therefore, the evolution

of permeability in the post-peak unloading failure stage is one of the focuses in this paper.

In this study, an approach is proposed to analyze the interaction among stress, strain and gas flow around a borehole. Main works contain following five components. First, analytical solutions of stress and strain around a borehole are developed after considering the coal compaction in the elastic zone. Then, a new permeability model is proposed for post-peak unloading failure stage. Third, the analytical solutions of stress and strain and the permeability model for post-peak unloading are used to calculate the distribution of stress, strain, and permeability around the borehole. The gas flow equation is numerically solved to obtain the gas distribution. The gas content predicted by this approach is then verified by two sets of field data. Fourth, parametric study is conducted to investigate the effect of the damage enhancement coefficient, initial geostress, drilling volume, and uniaxial strength on the gas pressure profile and the permeability around the borehole. Finally, the zoning of permeability and pore pressure is discussed. This study can provide a basis for a fast evaluation of drilling effect on permeability evolution and pore pressure distribution.

Analytical solutions of stress and strain in coal around a borehole

### Constitutive model with strain-softening behaviors

The underground drilling disturbs the rock nearby the newly formed cavity. After drilling, the surrounding rock usually experiences strain softening and forms three stress zones which correspond to the three stages in Fig. 1a. As shown in Fig. 2, R_0, R_b and R_p are the radii of the borehole, residual state zone and strain-softening zone, respectively.

At the pre-peak deformation stage, the rock is usually in the elastic stage (I) and few damage is observed (Peng et al. 2015). In the plastic-softening stage (II), the slope of curve k_s reflects the softening extent of rock (Brown et al. 1983; Lu and Yang 2013). This slope can be calculated from conventional triaxial compression tests. For an ideal elastic–plastic rock, $k_s = 0$. If Mohr–Coulomb yield function is applicable, the stresses in the post-peak zone satisfy

$$\sigma_\theta^p = k_p \sigma_r^p + \sigma_c^p, \tag{1}$$

where σ_θ^p and σ_r^p are the hoop and radial stress components in the strain-softening zone, respectively. $k_p = \tan^2(45° - \varphi/2)$, where φ is the internal friction angle of coal in that zone. σ_c^p is the compressive strength. When rock enters the residual stress stage, $\sigma_c^p = \sigma_c^*$. σ_c^* is the uniaxial residual strength. Generally, the uniaxial compressive strength in the unloading zone can be expressed by
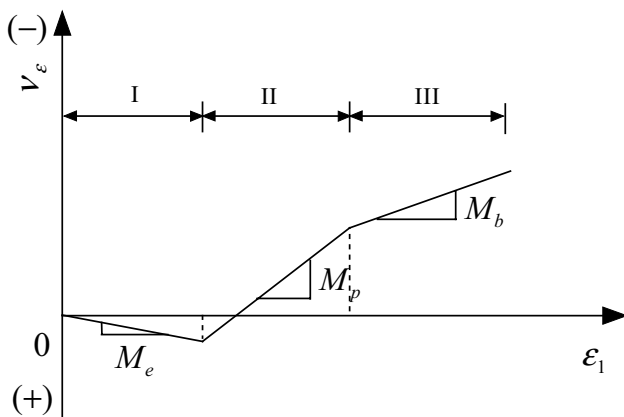
$$\sigma_c^p = \sigma_c - k_s E \left[\varepsilon_\theta^p - \varepsilon_\theta^e \big|_{r=R_p} \right], \tag{2}$$
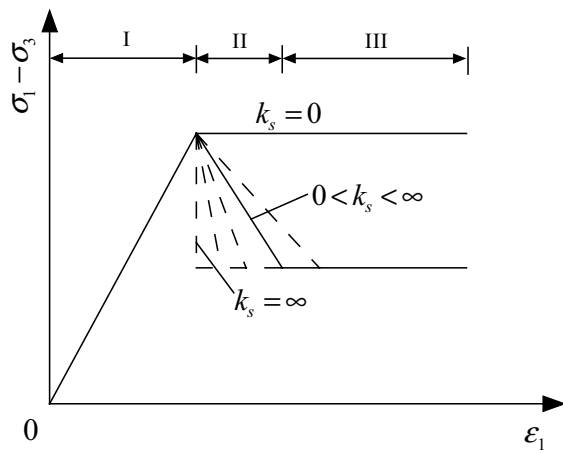
(a) $(\sigma_1 - \sigma_3) - \varepsilon_1$ curve
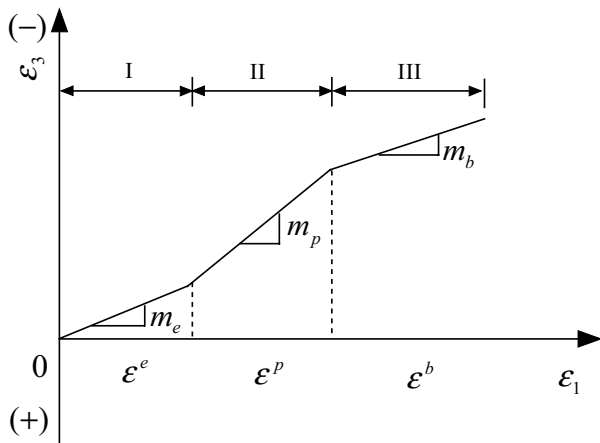
(b) $\varepsilon_3 - \varepsilon_1$ curve

(c) $\nu_\varepsilon - \varepsilon_1$ curve

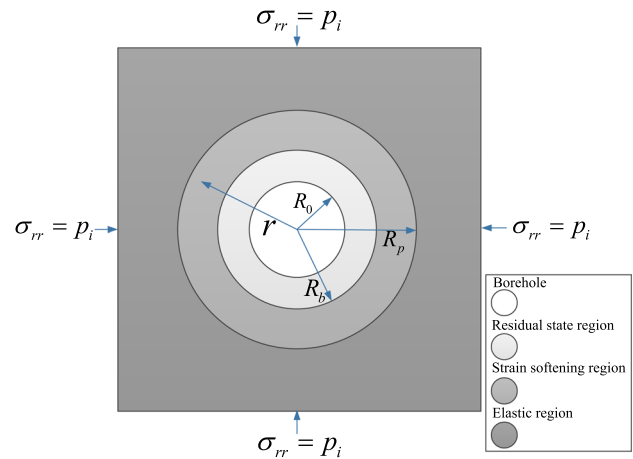**Fig. 1** Simplified three stepwise curve of rock (Brown et al. 1983)

Fig. 2 Illustration of three zones due to excavation or drainage drilling

where E is the Young's modulus. The superscripts "p" and "e" refer to plastic and elastic parts, respectively.

The dilatancy of rock is intensive in the post-peak zone. The dilatancy is widely expressed by (Brown et al. 1983; Lu and Yang 2013)

$$\Delta\varepsilon_r + m\Delta\varepsilon_\theta = 0, \tag{3}$$

where $\Delta\varepsilon_r$ and $\Delta\varepsilon_\theta$ are the increments of radial strain and hoop strain in the strain softening and residual state zones, respectively. The value for $m > 1$ represents the dilatancy extent. $m = 1.0$ indicates no dilation. As shown in Fig. 1b, the m is denoted as m_p in the strain-softening zone and as m_b in the residual state zone.

These studies are based on elastic–perfectly plastic or elastic–brittle–plastic or three step–wise models, thus rock is in the elastic zone before peak stress or strength. The volumetric strain curve was shown in Fig. 1c by Brown et al. (1983), but his elastic theory induced zero volumetric strain in this elastic zone. This is not the case for rock because the volumetric compaction is observed in the elastic zone. Volumetric strain is observed to decrease slightly in the elastic zone due to compaction and to increase dramatically in the post-peak zone due to dilatancy (Yin et al. 2013; Wang et al. 2013). This paper will extend Eq. (3) to include the compaction in the elastic zone when the m is specified as $m < 1$. This m is denoted as m_e. Therefore, the increment of volumetric strain is

$$\Delta\nu_\varepsilon = \Delta\varepsilon_r + \Delta\varepsilon_\theta = (1 - m)\Delta\varepsilon_\theta = M\Delta\varepsilon_\theta, \tag{4}$$

where $M = 1 - m$ has different value in each zone as shown in Fig. 1c.

Stress and strain in the elastic zone

The equilibrium equation in polar coordinates is

$$\frac{\partial \sigma_r}{\partial r} + \frac{\sigma_r - \sigma_\theta}{r} = 0. \tag{5}$$

For an axisymmetric problem with infinitesimal deformation, strain components can be expressed by radial displacement u_r as

$$\varepsilon_r = -\frac{du_r}{dr}, \quad \varepsilon_\theta = -\frac{u_r}{r}. \tag{6}$$

where r is the radial distance from the center.

The stress in the elastic zone is expressed as (Brown et al. 1983; Lu and Yang 2013):

$$\sigma_r^e = p_i - (p_i - \sigma_{R_p})\left(\frac{R_p}{r}\right)^2, \tag{7}$$

$$\sigma_\theta^e = p_i + (p_i - \sigma_{R_p})\left(\frac{R_p}{r}\right)^2, \tag{8}$$

where p_i is the initial stress, R_p is the boundary between the strain softening zone and the elastic zone, σ_{R_p} is the pressure on the boundary between the strain softening zone and the elastic zone and $\sigma_{R_p} = \frac{2p_i - \sigma_c}{k_p + 1}$.

Considering the shear stress-induced compaction of rock in the elastic zone, a dilatancy term is introduced into the constitutive law through the maximum shear stress of $\tau = \frac{1}{2}(\sigma_\theta^e - \sigma_r^e)$. The strain in the elastic zone is gotten as

$$\varepsilon_r^e = \frac{1-\mu^2}{E}\left(\Delta\sigma_r^e - \frac{\mu}{1-\mu}\Delta\sigma_\theta^e\right)\left(\frac{R_p}{r}\right)^{m_e-1} + \frac{1-m_e}{1+m_e}\frac{1+\mu}{E}\frac{1}{2}(\sigma_\theta^e - \sigma_r^e)\left(\frac{R_p}{r}\right)^{m_e-1}, \tag{9}$$

$$\varepsilon_\theta^e = \frac{1-\mu^2}{E}\left(-\frac{\mu}{1-\mu}\Delta\sigma_r^e + \Delta\sigma_\theta^e\right)\left(\frac{R_p}{r}\right)^{m_e-1} + \frac{1-m_e}{1+m_e}\frac{1+\mu}{E}\frac{1}{2}(\sigma_\theta^e - \sigma_r^e)\left(\frac{R_p}{r}\right)^{m_e-1}. \tag{10}$$

The strain is simplified as

$$\varepsilon_r^e = -m_e H\left(\frac{R_p}{r}\right)^{m_e+1}, \tag{11}$$

$$\varepsilon_\theta^e = H\left(\frac{R_p}{r}\right)^{m_e+1}, \tag{12}$$

where $H = 2(1+\mu)[(k_p - 1)p_0 + \sigma_c]/[E(k_p + 1)(1 + m_e)]$.

The volumetric strain v^e in this elastic zone is

$$v^e = \varepsilon_r^e + \varepsilon_\theta^e = (1 - m_e)\varepsilon_\theta^e = (1 - m_e)H\left(\frac{R_p}{r}\right)^{m_e+1}. \tag{13}$$

The displacement in the elastic zone is expressed as

$$u^e = H\frac{R_p^{m_e+1}}{r^{m_e}}. \tag{14}$$

Stress and strain in the strain-softening zone

Both elastic zone and strain-softening zone have the same strain at their boundary. The strain in the strain-softening zone is expressed as

$$\varepsilon_r^p = \varepsilon_r^e\big|_{r=R_p} + \Delta\varepsilon_r^p, \quad \varepsilon_\theta^p = \varepsilon_\theta^e\big|_{r=R_p} + \Delta\varepsilon_\theta^p. \tag{15}$$

The solutions for strain and displacement in the strain softening zone are obtained as follows after the combination of Eqs. (15) and (6) with Eq. (3):

$$u^p = Hr\left\{1 + \frac{2}{1+m_p}\left[\left(\frac{R_p}{r}\right)^{1+m_p} - 1\right]\right\}, \tag{16}$$

$$\varepsilon_r^p = -H\left\{m_e + \frac{2m_p}{1+m_p}\left[\left(\frac{R_p}{r}\right)^{1+m_p} - 1\right]\right\}, \tag{17}$$

$$\varepsilon_\theta^p = H\left\{1 + \frac{2}{1+m_p}\left[\left(\frac{R_p}{r}\right)^{1+m_p} - 1\right]\right\}. \tag{18}$$

Therefore, the volumetric strain of v^p is

$$\begin{aligned} v^p &= \varepsilon_r^p + \varepsilon_\theta^p = (1 - m_e)\varepsilon_r^e + (1 - m_p)\Delta\varepsilon_\theta^p \\ &= H\left\{1 - m_e + \frac{2(1-m_p)}{1+m_p}\left[\left(\frac{R_p}{r}\right)^{1+m_p} - 1\right]\right\}. \end{aligned} \tag{19}$$

Combining Eqs. (2), (5), (18), (12) with boundary condition $\sigma_r^e\big|_{r=R_p} = \sigma_r^p\big|_{r=R_p}$, the stress in the strain softening zone is expressed as (Yuan and Chen 1986)

$$\sigma_r^p = \frac{2}{k_p+1}\left[p_0 + \frac{\sigma_c}{k_p-1} + \frac{(k_p+1)k_sEH}{(k_p-1)(k_p+m_p)}\right]\left(\frac{r}{R_p}\right)^{k_p-1} + \frac{2k_sEH}{1+m_p}\left[\frac{1}{k_p+m_p}\left(\frac{R_p}{r}\right)^{1+m} - \frac{1}{k_p-1}\right] - \frac{\sigma_c}{k_p-1},$$
(20)

$$\sigma_\theta^p = k_p\sigma_r^p + \sigma_c - \frac{2k_sEH}{1+m_p}\left[\left(\frac{R_p}{r}\right)^{1+m_p} - 1\right].$$
(21)

Stress and strain in the residual state zone

The strain in the residual state zone is the summation of the strain in the residual state zone and the strain at the boundary between strain-softening zone and residual state zone:

$$\varepsilon_r^b = \varepsilon_r^p\big|_{r=R_b} + \Delta\varepsilon_r^b, \ \varepsilon_\theta^b = \varepsilon_\theta^p\big|_{r=R_b} + \Delta\varepsilon_\theta^b.$$
(22)

Similarly, combining Eqs. (6), (22) with Eq. (3) obtains the strain and the radial displacement in the residual state zone as

$$u^b = 2rH\left\{\left\{\frac{1}{1+m_p} + \frac{1}{1+m_b}\left[\left(\frac{R_b}{r}\right)^{1+m_b} - 1\right]\right\}\left(\frac{R_p}{R_b}\right)^{1+m_p} + \frac{m_p-1}{2(m_p+1)}\right\},$$
(23)

$$\varepsilon_r^b = -2H\left\{\left\{\frac{m_p}{1+m_p} + \frac{m_b}{1+m_b}\left[\left(\frac{R_b}{r}\right)^{1+m_b} - 1\right]\right\}\left(\frac{R_p}{R_b}\right)^{1+m_p} + \frac{m_e}{2} - \frac{m_p}{m_p+1}\right\},$$
(24)

$$\varepsilon_\theta^b = 2H\left\{\left\{\frac{1}{1+m_p} + \frac{1}{1+m_b}\left[\left(\frac{R_b}{r}\right)^{1+m_b} - 1\right]\right\}\left(\frac{R_p}{R_b}\right)^{1+m_E} + \frac{m_p-1}{2(m_p+1)}\right\}.$$
(25)

The volumetric strain v^b in the residual state zone is

$$v^b = \varepsilon_r^b + \varepsilon_\theta^b = 2H\left\{\left\{\frac{1-m_p}{1+m_p} + \frac{1-m_b}{1+m_b}\left[\left(\frac{R_b}{r}\right)^{1+m_b} - 1\right]\right\}\left(\frac{R_p}{R_b}\right)^{1+m_p} - \frac{m_e}{2} + \frac{3m_p-1}{2(m_p+1)}\right\}.$$
(26)

The Mohr–Coulomb criterion in the residual state zone can be expressed as

$$\sigma_\theta^p = k_p\sigma_r^p + \sigma_c^*,$$
(27)

where σ_c^* is the uniaxial residual strength.

The stresses in the residual state zone are obtained by solving Eqs. (5), (27) with the boundary condition $\sigma_r^p\big|_{r=R_b} = \sigma_r^b\big|_{r=R_b}$. They are

$$\sigma_r^b = \left\{\frac{2}{k_p+1}\left[p_0 + \frac{\sigma_c}{k_p-1} + \frac{(k_p+1)k_sEH}{(k_p-1)(k_p+m_p)}\right]\left(\frac{R_b}{R_p}\right)^{k_p-1} - \frac{2k_sEH + (1+m_p)(\sigma_c-\sigma_c^*)}{(k_p-1)(k_p+m_p)}\right\}\left(\frac{r}{R_b}\right)^{k_p-1} - \frac{\sigma_c^*}{k_p-1},$$
(28)

$$\sigma_\theta^b = k_p\sigma_r^b + \sigma_c^*.$$
(29)

Radius of strain-softening zone and residual state zone

According to Eqs. (20), (28), at the boundary between the strain-softening zone and the residual state zone R_b, $\sigma_r^b\big|_{r=R_b} = \sigma_r^p\big|_{r=R_b}$, the relationship between R_p and R_b is obtained as

$$R_p = R_b\left[1 + \frac{(1+m_p)(\sigma_c-\sigma_c^*)}{2k_sEH}\right]^{\frac{1}{1+m_p}}.$$
(30)

The radius of strain-softening zone R_b is obtained by Eq. (28) with $r = R_0$ and $\sigma_r^b = p_s$, p_s is the supporting traction of cavity. The supporting force exists for the roadway when the supporting measures are adopted. The supporting

force is $p_s = 0$ for boreholes during coalbed methane (CBM) drilling. The final expression is

$$
R_b = R_0 \left\{ \left\{ \frac{2}{k_p + 1} \left[p_i + \frac{\sigma_c}{k_p - 1} + \frac{(k_p + 1)k_s EH}{(k_p - 1)(k_p + m_p)} \right] \left[\frac{2k_s EH}{2k_s EH + (1 + m_p)(\sigma_c - \sigma_c^*)} \right]^{\frac{k_p - 1}{1 + m_p}} \right. \right.
$$
$$
\left. \left. - \frac{2k_s EH + (1 + m_p)(\sigma_c - \sigma_c^*)}{(k_p - 1)(k_p + m_p)} \right\} \middle/ \left(p_s + \frac{\sigma_c^*}{k_p - 1} \right) \right\}^{\frac{1}{k_p - 1}}.
$$

(31)

After the radii of the strain softening and the residual state zones are obtained by Eqs. (30) and (31), the stresses around a borehole can be finally obtained by Eqs. (7), (8), (20), (21), (28) and (29) and the volumetric strains can be finally calculated by Eqs. (13), (19) and (26).

Permeability evolution of coal at post-peak failure stage

A brief review of permeability of coal at post-peak failure stage

In the process of coal mining and gas extraction, the fracture of coal changes significantly due to the release of both radial and hoop stresses and thus the permeability of coal seam increases dramatically due to excavation or CBM drilling. According to the experiments conducted by Pan et al. (2014) and Chu et al. (2017), Fig. 3 is drawn to present the change of permeability along four loading paths, where curve 1 presents the loading path and curve 2 denotes the pre-peak unloading path in elastic zone. Both curves 1 and 2 are coincided because of elastic deformation. Curve 3 presents the pre-peak unloading of elastic–plastic materials because plastic deformation is irrecoverable. Finally, curve 4 presents the post-peak unloading path. Obviously, curve 4 has special property compared to other three paths.

Each curve represents different physical mechanisms. The permeability changes along curve 1 for loading and along curve 2 for unloading. Due to reversible deformation, curves 1 and 2 are identical. During loading process, permeability decreases with the increase of stress due to coal compaction. The deformation resisting capability of fracture surface is developed and the decreasing trend of permeability slows down. When stress is unloaded, the permeability increases due to the release of whole coal structure. Both curves for loading and unloading are coincided due to elastic deformation. For the coal with elastic–plastic model, permeability increases with unloading (see curve 3). The unloading process is irreversible process. It is difficult for a closed fracture in loading process to be recovered completely in unloading process.

Thus the permeability is smaller than that in loading process. It is also noted that the permeability increases very fast when stress is small. As seen in curve 4, the coal swells significantly in the post-peak unloading. This significantly enhances the permeability in this stage. This unloading destructs the coal microstructures and generates a large amount of new cracks. Stress drops until the residual stress state where the coal is seriously damaged. Simultaneously, the permeability is rapidly enhanced. The gas is more easily released from the fractured coal. This causes higher gas emission and thereby increases the gas content to its limit and even induces coal and gas outburst. Therefore, the permeability model is the critical to the control of coal and gas outburst and each loading path has its evolution of permeability.

Evolution of coal porosity and permeability

The bulk volume of the porous medium is $V = V_p + V_s$ and its porosity is $\phi = V_p/V$. The volumetric strain and the pore-volumetric strain are expressed by

$$
\frac{\Delta V}{V} = -\frac{1}{K}(\sigma - \alpha p) + \varepsilon_s,
$$

(32)

$$
\frac{\Delta V_p}{V_p} = -\frac{1}{K}(\sigma - \beta p) + \varepsilon_s,
$$

(33)

where α is the Biot coefficient and $\beta = 1 - K_p/K_s$. K_p is the modulus of pores. σ, p are the total hydrostatic stress and
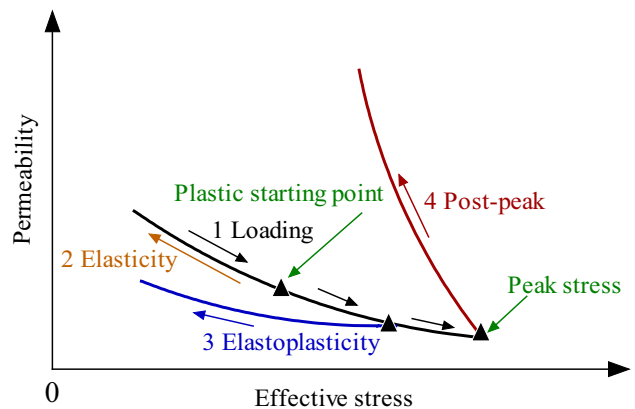

Fig. 3 Permeability evolution of coal with loading and unloading

pore pressure, respectively. ε_s is the sorption–induced swelling strain.

Thus, the change of porosity is calculated by

$$d\phi = d\left(\frac{V_p}{V}\right) = \frac{V_p}{V}\left(\frac{dV_p}{V_p} - \frac{dV}{V}\right). \tag{34}$$

Integrating Eq. (34) yields

$$\frac{\phi}{\phi_0} = \exp\left\{\left(\frac{1}{K} - \frac{1}{K_p}\right)[(\sigma - \sigma_0) - (p - p_0)]\right\}. \tag{35}$$

The permeability change law is obtained by (Cui and Bustin 2005)

$$k = k_0\left(\frac{\phi}{\phi_0}\right)^3 = k_0\exp\left\{3\left(\frac{1}{K} - \frac{1}{K_p}\right)[(\sigma - \sigma_0) - (p - p_0)]\right\}. \tag{36}$$

This formula is more suitable for elastic deformation. The relationship between the permeability and effective stress can be expressed as (Shi and Durucan 2004; Pan and Connell 2011; Salmachi et al. 2013)

$$k = k_0 e^{-3c_f(\sigma - \sigma_0)}, \tag{37}$$

where k_0 is the initial permeability; c_f is the cleat compressibility. This permeability model describes the permeability evolution of the coal without damage.

Assuming that the length of the fracture traces per unit area of the trace plane is P_1 and the area of fractures per unit volume of rock is P_2, the fracture porosity of the coal can be expressed as $\phi = bP_2$. Then, the permeability can be rewritten as

$$k = \frac{P_1}{\tau P_2^3}\frac{\phi^3}{12}, \tag{38}$$

where τ is the tortuosity parameter; b is the fracture aperture.

Differentiating the fracture permeability with respect to the effective stress results in

$$\frac{\partial k}{\partial \sigma_e} = \frac{P_1}{\tau P_2^3}\frac{\phi^2}{4}\frac{\partial \phi}{\partial \sigma_e}. \tag{39}$$

Incorporating Eq. (39) into (38), we have

$$\frac{\partial k}{\partial \sigma_e} = 3D_f k, \tag{40}$$

where $D_f = \frac{1}{\phi}\frac{\partial \phi}{\partial \sigma_e}$, which denotes the change in the fracture porosity of damaged coal in different stress states.

A damage variable D was introduced to take into consideration the degeneration of elasticity modulus (Brown et al. 1983; Yang and Baleanu 2013)

$$D = 1 - E/E_0, \tag{41}$$

where E is the elastic modulus of coal samples under different stress states, and E_0 is the initial elastic modulus of the coal samples.

The damage variable D can be used to describe the development degree of fractures in the coal samples (Peng et al. 2015; Zhu et al. 2013, 2018). Therefore, the following equation can be used to describe the relationship between these two variables

$$D_f = \gamma D, \tag{42}$$

where γ is the coefficient, which reflects the sensitivity degree of the fracture development to the effective stress.

Thus, Eq. (40) can be expressed as

$$\frac{\partial k}{\partial \sigma_e} = 3\gamma D k. \tag{43}$$

When $\lambda = -\gamma/c_f$, Eq. (43) can be expressed as (Xue et al. 2016)

$$k = k_0 e^{-3c_f\lambda D(\sigma_e - \sigma_{e0})}, \tag{44}$$

where k_0 is the initial permeability, c_f is the compression coefficient of fracture, λ is the damage enhancement coefficient, which reflects the influence coefficient of damage to permeability, σ_e is the effective stress. More detailed description about this equation can be referred in Xue et al. (2016).

An approach for the couplings among stress, strain and gas flow

Gas flow equation

The mass conservation law of gas is

$$\frac{\partial m}{\partial t} + \nabla \cdot (\rho_g \vec{q}_g) = Q_m\}, \tag{45}$$

where ρ_g is the gas density, $\vec{q}_g$ is the velocity, Q_m is the source, and m is the gas content which calculated through the Langmuir equation (Saghafi et al. 2007),

$$m = \rho_g \phi + \rho_{ga}\rho_c\frac{V_L p}{p + p_L}, \tag{46}$$

where ρ_g is the gas density, ρ_{ga} is the gas density at standard conditions, ρ_c is the coal density, ϕ is the coal porosity, V_L denotes the adsorption capacity of coal, and P_L denotes the Langmuir pressure constant.

After ignoring the gravity, the Darcy velocity of $\vec{q}_g$ is given by (Yarmohammadtooski et al. 2017)

$$\vec{q}_g = -\frac{k}{\mu}\nabla p, \tag{47}$$

where k is the coal permeability and μ is the dynamic viscosity. Substituting Eqs. (46) into (45), the equation of gas flow is

$$\left[\phi + \frac{\rho_c p_a V_L p_L}{(p + p_L)^2} \right] \frac{\partial p}{\partial t} + p \frac{\partial \phi}{\partial t} - \nabla \cdot \left(\frac{k}{\mu} p \nabla p \right) = Q_m. \quad (48)$$

Computation procedure of the approach

The deformation and the stress redistribution nearby a borehole and the formation of post-peak failure zone are mainly induced by drilling process while the influence of gas flow within coal seam on these changes is slight (Adhikary and Guo 2015; Borisenko 1985). On the other hand, coal deformation and crack propagation at the post-peak failure stage are mainly governed by stress redistribution. The deformation and stress redistribution have significant impacts on permeability evolution and gas pressure profile. The approach should take this impact of stress redistribution on permeability and gas pressure into account. Based on this understanding, an approach as described in Fig. 4a is proposed in this paper. Particularly, the effect of deformation and stress on porosity and permeability is carefully considered in the calculation of gas flow. In this case, the above analytical solutions of stress and strain are used to calculate their impact on porosity and permeability.

This approach adopts the following computational procedure: First, the analytical solutions of stress and strain are used to compute the stress and strain in each zone and to determine the size of each zone. Then, the permeability model is used to calculate the permeability distribution in each zone. That is, the pre-peak permeability model (Cui–Bustin model) is applied to the elastic zone and the post-peak permeability model is applied to both strain-softening and residual state zones (Fig. 4b). Finally, the gas flow equation is numerically solved based on the porosity and permeability in each zone.

The coal matrix swelling affects the permeability of the undamaged coal mass significantly. We consider the coal matrix swelling in pre-peak stage by adopting the Cui–Bustin model in pre-peak stage. For the fractured coal mass in post-peak failure stage, the gas sorption-induced strain is usually less than 5×10^{-4} (Liu et al. 2010) and the overall volumetric strain is normally larger than 1.5×10^{-2} (Chen et al. 2016). The total volumetric strain of the coal increases substantially due to the excavation-induced damage in the post-failure stage, even with the emergence of macro-fracture and large deformation, while the gas sorption-induced strain accounts for a small percentage of the overall volumetric strain. Therefore, we consider the coal matrix swelling in pre-peak stage and ignore it in the post-peak failure stage, with referring the approach proposed by Chen et al. (2016).

A one-dimensional numerical model is established, as shown in Fig. 5. The length of the model is 100 m. The initial gas pressure in the coal seam is 1.5 MPa and the cavity to represent the borehole is 50 mm in radius. The pressure will remain constant at a large distance from the well, thus the boundary condition may be approximated as follows (Liu et al. 2015):

$$p = p_0 \text{ at } r = R_c, \quad (49)$$

where $r = R_c$ is the radius of the whole analyzed zone. The extraction pressure of the borehole is

$$p = p_a \text{ at } r = R_0, \quad (50)$$
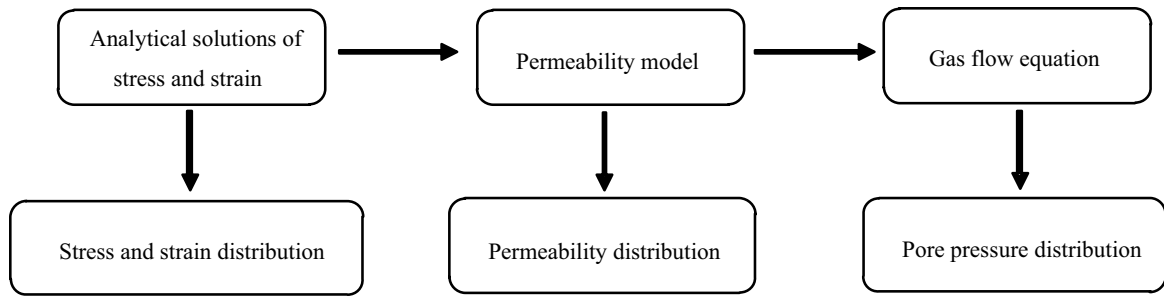
where $r = R_0$ is the radius of the borehole.

After the borehole is drilled, the gas flows from coal seam to borehole. Other computational parameters are listed in Table 1. The nonlinear partial differential equation (PDE) solver within the framework of COMSOL Multiphysics is employed to solve the gas flow equation, and the analytical solutions for deformation and stress are input into the COMSOL.
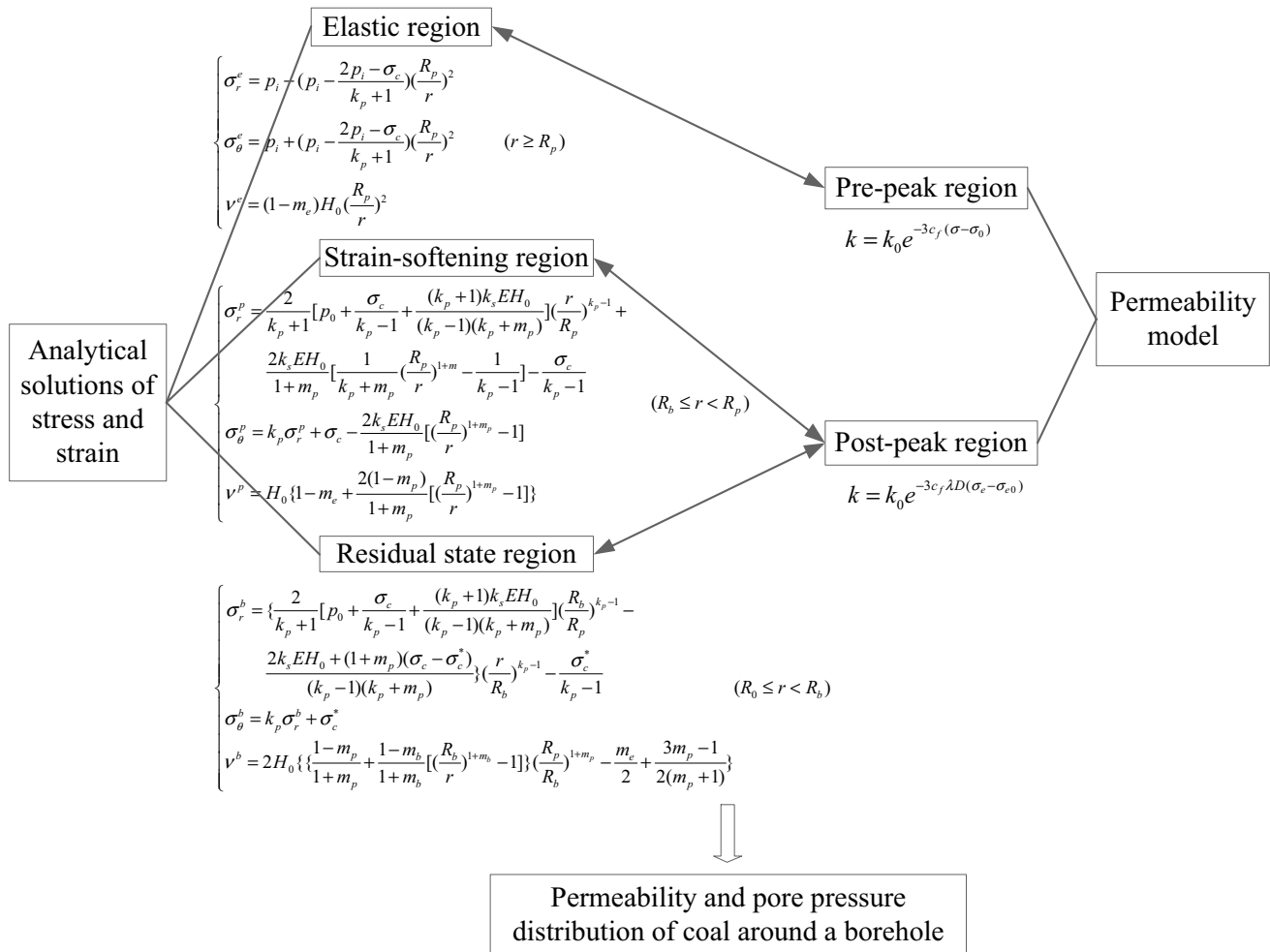
Model validation

Verification by field data

This approach is verified through the comparison with the field data obtained from the No.8 seam in Shoushan mine of the Pingmei Corporation, China. The No.8 coal seam has the gas outburst hazard with a gas pressure of 0.32–0.78 MPa and a gas content of 3.26–6.52 m^3/t. The validity of the model can be directly verified by measuring the gas pressure at different positions of the coal seam. However, because of the difficulty in measuring gas pressure, we adopted gas content as the comparison parameter instead of gas pressure. We measured the gas content distribution of coal seam at the time of 135 days after roadway excavation according to the determination method for underground gas content (State Administration of Coal Mine Safety of China 2006). The gas content was measured every 1 m along the excavation wall of roadway from the depth of 1 m.

A similar physical model to Fig. 5 is established. The initial gas pressure in the coal seam is 0.78 MPa and the cavity to represent the roadway is 2.7 m in radius. The same boundary conditions are used in the calculation, as show in Fig. 5. Following parameters are used to calculate the gas content distribution of coal seam after excavation. The initial geo-stress is 11.95 MPa. The roadway was supported with bolt mesh and the support pressure is 0.15 MPa. The initial gas pressure is 0.78 MPa; CH_4 Langmuir pressure constant is 6.1 MPa; CH_4 Langmuir volume constant is 0.02 m^3/kg; CH_4 Langmuir volumetric

Analytical solutions of stress and strain → Permeability model → Gas flow equation

Stress and strain distribution   Permeability distribution   Pore pressure distribution

(a) Coupling approach

Elastic region

$$\sigma_r^e = p_i + (p_i - \frac{2p_i - \sigma_c}{k_p+1})(\frac{R_p}{r})^2$$

$$\sigma_\theta^e = p_i + (p_i - \frac{2p_i - \sigma_c}{k_p+1})(\frac{R_p}{r})^2 \qquad (r \geq R_p)$$

$$v^e = (1-m_e)H_0(\frac{R_p}{r})^2$$

Pre-peak region

$$k = k_0 e^{-3c_f(\sigma-\sigma_0)}$$

Permeability model

Strain-softening region

$$\sigma_r^p = \frac{2}{k_p+1}[p_0 + \frac{\sigma_c}{k_p-1} + \frac{(k_p+1)k_sEH_0}{(k_p-1)(k_p+m_p)}](\frac{r}{R_p})^{k_p-1} +$$
$$\frac{2k_sEH_0}{1+m_p}[\frac{1}{k_p+m_p}(\frac{R_p}{r})^{1+m} - \frac{1}{k_p-1}] - \frac{\sigma_c}{k_p-1}$$

$$\sigma_\theta^p = k_p\sigma_r^p + \sigma_c - \frac{2k_sEH_0}{1+m_p}[(\frac{R_p}{r})^{1+m_p}-1]$$

$$v^p = H_0\{1-m_e + \frac{2(1-m_p)}{1+m_p}[(\frac{R_p}{r})^{1+m_p}-1]\}$$

$(R_b \leq r < R_p)$

Post-peak region

$$k = k_0 e^{-3c_f\lambda D(\sigma_e-\sigma_{e0})}$$

Residual state region

$$\sigma_r^b = \{\frac{2}{k_p+1}[p_0 + \frac{\sigma_c}{k_p-1} + \frac{(k_p+1)k_sEH_0}{(k_p-1)(k_p+m_p)}](\frac{R_b}{R_p})^{k_p-1} -$$
$$\frac{2k_sEH_0+(1+m_p)(\sigma_c-\sigma_c^*)}{(k_p-1)(k_p+m_p)}\}(\frac{r}{R_b})^{k_p-1} - \frac{\sigma_c^*}{k_p-1} \qquad (R_0 \leq r < R_b)$$

$$\sigma_\theta^b = k_p\sigma_r^b + \sigma_c^*$$

$$v^b = 2H_0\{\{\frac{1-m_p}{1+m_p} + \frac{1-m_b}{1+m_b}[(\frac{R_b}{r})^{1+m_b}-1]\}(\frac{R_p}{R_b})^{1+m_p} - \frac{m_e}{2} + \frac{3m_p-1}{2(m_p+1)}\}$$

Permeability and pore pressure distribution of coal around a borehole

(b) Formulae used in each process

Fig. 4 Flowchart for computational procedure of the approach

strain constant is 0.023. Other parameters are derived from Table 1. Figure 6 presents the comparison between our simulations with the field data. This figure shows that the approach can reliably predict the gas content nearby the newly formed cavity. Therefore, this approach is applicable to gas flow problem around a borehole.

Fig. 5 One-dimensional physical model
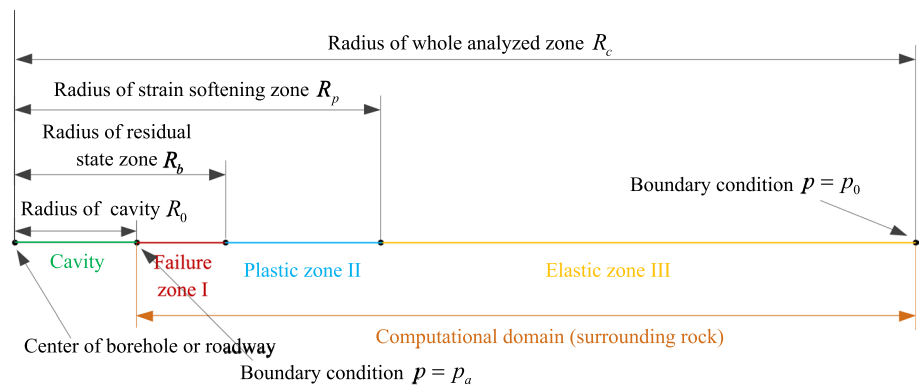
Numerical validation

In this section, we further examine the effectiveness of this approach in simulating the gas flow around the cavity. We compared our approach with the fully coupled hydro-mechanical model of Xue et al. (2018). The coupled governing equation for coal seam deformation and gas flow in the model of Xue et al. (2018) are expressed as:

$$Gu_{i,jj} + \frac{G}{1-2\mu}u_{j,ji} - \alpha p_i - K\varepsilon_{s,i} + f_i = 0, \tag{51}$$

$$\left[\phi + \frac{\rho_c p_a V_L p_L}{(p + p_L)^2}\right]\frac{\partial p}{\partial t} + p\frac{\partial \phi}{\partial t} - \nabla \cdot \left(\frac{k}{\mu}p\nabla p\right) = Q_m. \tag{52}$$

The physical model is same as the model in "Computation procedure of the approach" and the same parameters are used in the calculation. A comparison of the pressure distribution and permeability distribution along the radial direction at 10^7 s is shown in Fig. 7. It can be seen from Fig. 7 that there is a good agreement between these two solutions, which further verifies the effectiveness of the approach proposed in this paper.

Parametric study on the approach

The approach is applied to the analysis of stress, strain, gas pressure and permeability distribution around a borehole through parametric study. This study is to understand the accumulation of gas content around the borehole and to explore the mechanism of gas accumulation. The base computation parameters are listed in Table 1. Each time changes only parameter from the base parameters. The effects of following parameters on permeability and gas distribution are investigated: permeability enhancement coefficient, initial geo-stress, drilling size, and uniaxial strength.

Distribution of stress and volumetric strain

Based on the computation parameters in Table 1, the radii are obtained as $R_b = 71.83$ mm for the residual state zone and $R_p = 89.83$ mm for the strain softening zone. Figure 8 presents the stress distribution along radial direction after drilling. The distance is measured from the center of circular borehole. The drilling surface is free of traction, thus the radial stress on the wall drops to almost zero. The radial stress gradually increases and approaches towards the initial in situ stress with further distance from the wall of the hole. However, the hoop stress at the coal wall immediately drops to a low stress level (residual state) after drilling. This stress rises with further distance from the wall and approaches to a peak stress at the radius of strain-softening zone R_p. The stress concentration factor at this point is 1.87. This stress concentration factor is the ratio of the mining–induced stress to the pre-mining in situ stress. It is found that this factor is in the range of 1.5–6 (Singh et al. 2011).

The change of volumetric strain along the radial distance is observed in Fig. 9. The volumetric strain decreases in the elastic zone due to coal compaction. In the plastic zone, dilatancy and damage are observed and the volumetric strain increases substantially. When $m_e = 0.8$, the volumetric strain reaches its minimum of $v_\varepsilon = -0.05\%$ at the radius of strain-softening zone $R_p = 89.83$ mm. The volumetric strain reaches its maximum of $v_\varepsilon = 0.48\%$ at the coal wall of borehole. If the compaction is not considered, that is $m_e = 1$, the volumetric strain in the elastic zone is $v_\varepsilon = 0$ but the maximum volumetric strain is still $v_\varepsilon = 0.48\%$ at coal wall. Therefore, coal compaction in elastic zone has some impact on the volumetric strain near the interface between strain-softening zone and elastic zone.
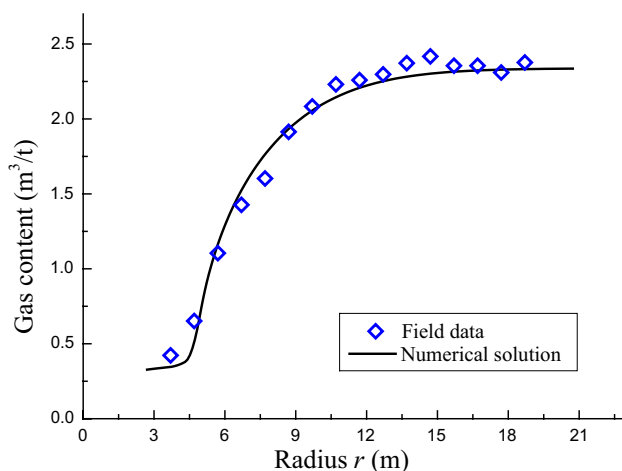
Table 1 Computational parameters for coal and gas

Parameter	Value
Uniaxial compressive strength of coal (σ_c, MPa)	9
Residual strength of coal (σ_c^*, MPa)	2
Young's modulus of coal (E, GPa)	2.7
Young's modulus of the coal grains, (E_s, GPa)	8.1
Initial geo-stress in coal seam (p_i, MPa)	11
Density of coal, (ρ_c, kg/m^3)	1250
Angle of internal friction of coal (φ, °)	30
Poisson ratio of coal (v, –)	0.22
Initial gas pressure in coal seam (p_0, MPa)	1.5
Extraction pressure (p_a, MPa)	0.1
Initial permeability of coal (k_0, m^2)	1×10^{-17}
Initial porosity of coal (ϕ_0, –)	0.008
Density of methane at standard conditions (ρ_{ga}, kg/m^3)	0.717
Gas dynamic viscosity (μ, N s/m^2)	1.84×10^{-5}
CH$_4$ Langmuir pressure constant (P_L, MPa)	7.2
CH$_4$ Langmuir volume constant (V_L, m^3/kg)	0.015
CH$_4$ Langmuir volumetric strain constant (ε_L, –)	0.013
Softening coefficient of coal (k_s, –)	1.5
Volume coefficient of coal in elastic region (m_e, –)	0.8
Volume coefficient of coal in strain-softening region (m_p, –)	2
Volume coefficient of coal in residual region (m_b, –)	1.5

Parametric study on permeability distribution

Effect of the damage enhancement coefficient on permeability

The effect of damage enhancement coefficient λ is observed in Fig. 10. The initial permeability of coal seam is specified as 1×10^{-17} m^2. The permeability keeps unchanged in the undisturbed rock which is far away from the borehole. In the elastic zone, the permeability decreases gradually to the minimum of 8.86×10^{-18} m^2 at the boundary of strain-softening zone and elastic zone. As the hoop stress increased with the decrease of distance from borehole, cracks close. The closing of cracks blocks flow channels and reduces the permeability. In the strain-softening zone, coal enters the post-peak failure stage. New cracks emerge in a large scale. This induces the rapid increase of permeability and the decline of coal strength. Finally, the coal enters the residual stress state where coal is fully fractured and has the highest permeability. When the damage is not considered, the maximum permeability is 1.11×10^{-17} m^2 which is 1.1 times of its initial permeability. When damage enhancement coefficient $\lambda = 1.5$, 4.5 and 6.5, the maximum permeability is 1.62×10^{-17} m^2, 1.07×10^{-15} m^2, and 2.26×10^{-14} m^2, respectively. When $\lambda = 4.5$, the maximum permeability of coal around borehole increases about 2 orders of magnitude due to drilling.

Effect of initial geo-stress on permeability

The impact of initial geo-stress on permeability is investigated. Initial geo-stress is assumed to be hydrostatic stress generated by the gravity of overlying strata. Figure 11 presents the permeability profile along the radial distance. This figure shows that the radii of both residual stress zone and strain-softening zone are larger for higher initial geo-stress. The unloading zone is larger and the permeability enhancement is higher. Therefore, higher initial geo-stress has larger unloading zone and higher permeability enhancement. This suggests that the permeability enhancement due to drilling increases with the increase of mining depth and thus the risk of coal and gas outburst is higher.
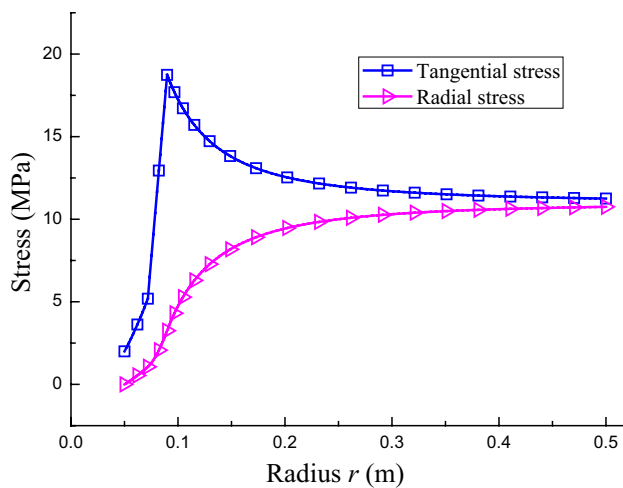

Fig. 6 Comparison of simulated gas content and field data
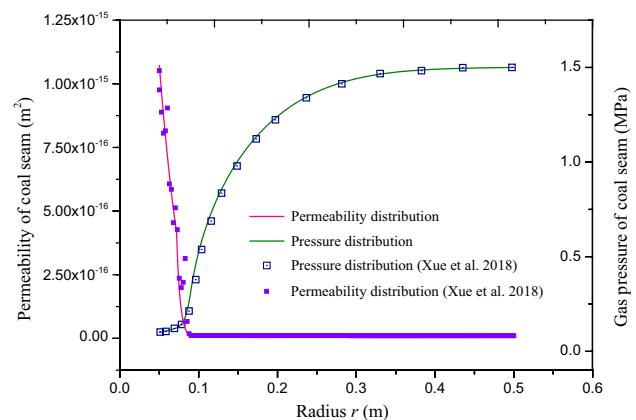
Fig. 7 Comparison with the numerical solution

Fig. 8 Stress distribution around borehole

Fig. 9 Change of volumetric strain with compaction coefficients around borehole

Effect of drilling size on permeability

The effect of drilling size on the permeability is explored. Figure 12 is the relationship between permeability and normalized distance from center. A unique relationship is observed regardless of drilling radius R_0. With the increase of drilling radius R_0, both the residual state zone and the strain softening zone are broadened. The ranges of unloading zone and the permeability enhancement zone are widened, too. However, permeability, hoop stress, radial stress and volumetric strain are only function of the normalized radius R/R_0 if the gravity is not considered. The permeability enhancement degree is also observed to be independent of drilling radius R_0. The drilling size only affects the range of permeability enhancement. The permeability enhancement is closely related to the mechanical property of coal seam and the geological condition of coal mine. In the excavation process of coal mine including gas drainage borehole, the coal around borehole and in front of working face experiences a post-peak failure process. Thus, the permeability in these zones is usually high. This may trigger gas outburst. Of course, gas outburst is a nonlinear dynamic disaster triggered by the combination of in situ stress, gas pressure and the change of mechanical properties of coal (Hu et al. 2015a, b; Jin et al. 2011). In situ stress, gas pressure, the mechanical properties of coal, and energy characteristic are the important factors in considerations when the risk of gas outbursts is evaluated.

Effect of uniaxial strength on permeability

The effect of failure strength of coal on permeability is investigated. Figure 13 presents the influence of uniaxial strength of coal on permeability. This figure shows that uniaxial strength has s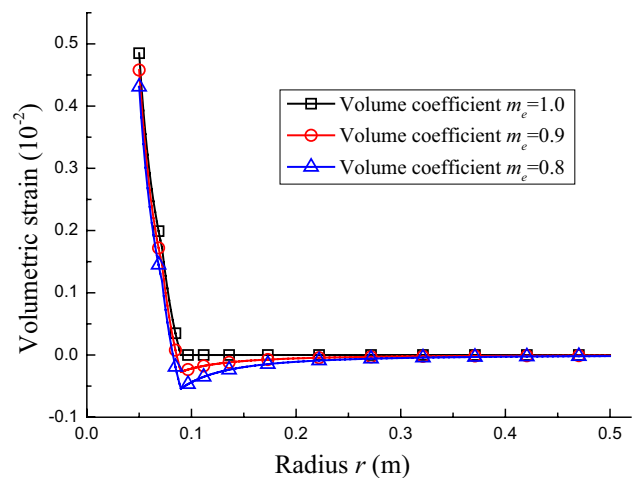ome impacts on the permeability only at the post-peak failure stage. When uniaxial strength of coal is lower, the zone of post-peak failure is larger and the permeability enhancement is greater. In coal mining, the physical properties of coal vary widely in different districts. Therefore, coal strength is an important factor to the excavation-induced permeability enhancement and the trigger of coal and gas outburst.

Gas pressure profile near borehole

The gas pressure profile is a crucial parameter for coal and gas outburst. Figure 14a presents the gas pressure distribution along radial distance from the borehole at different times. In computation, the coefficient $\lambda = 4.5$ and the gas pressure at the coal wall is 0.1 MPa. A high pressure gradient is observed near the boundary between strain-softening region and elastic region. This indicates poor permeability in this small zone. The gas cannot easily flow through this zone (Lin et al. 2010).

The effect of damage enhancement coefficient on gas profile is discussed here. Figure 14b presents the gas pressure profile at $t = 1 \times 10^7$ s when the coefficient $\lambda = 1.5$, 4.5 and 6.5. The gas pressure has a distribution of "slow–steep–slow" shape when $\lambda = 4.5$ and 6.5. When the λ is low, the permeability enhancement is not salient in the post-peak failure stage. Its gas velocity does not increase substantially. A smooth transition for the pressure curve is observed in the whole zone. The maximum gradient of pore pressure appears near the coal wall. When the λ is high such as 60 and 100, the permeability is pretty high in the post-peak failure zone. The maximum gradient is observed near the boundary of strain softening zone and elastic zone. This is the difference from those with low λ or no damage enhancement coefficient.
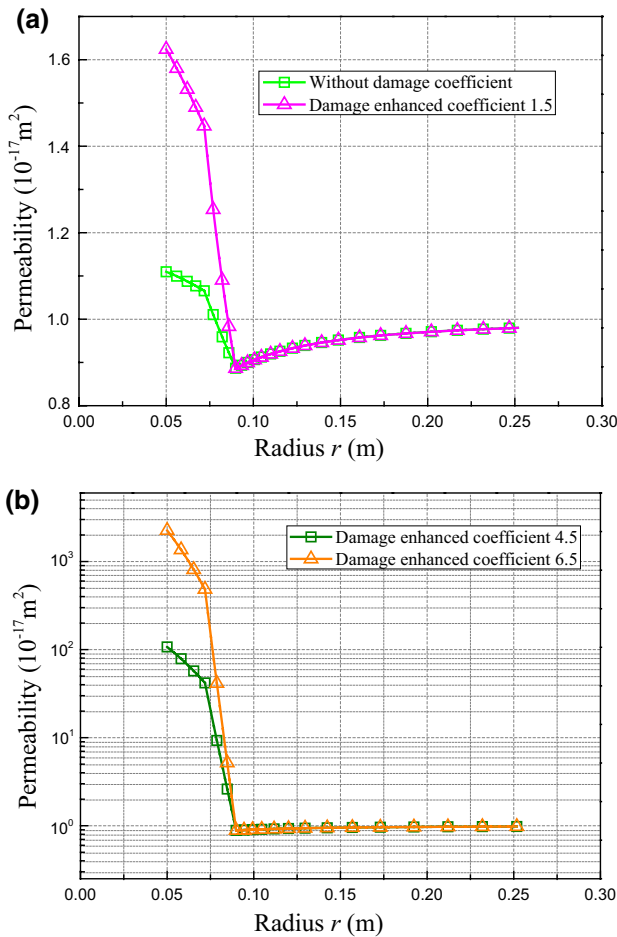
(a)

(b)

Fig. 10 Effect of the damage enhanced coefficient on permeability

Zoning of permeability and pore pressure

The distributions of stress, strain, permeability, and gas pressure are plotted together in Fig. 15. The data in Fig. 15 are obtained from Figs. 8, 9, 10, 11, 12, 13 and 14. The gas pressure curve is at $t = 1 \times 10^7$ s. These figures show that drilling leads to the stress redistribution around borehole. Three zones of elastic zone, strain softening zone and residual state zone are formed along the distance from the coal wall. They correspond to the three stages of stress–strain curve. After drilling, the coal wall (location a) is totally unconfined, the horizontal stress σ_r and the vertical stress σ_θ decline to the low value. With the increase of distance from the coal wall, the stress σ_r and σ_θ increase gradually. The coal between the locations a and b is at the post-peak failure stage. The coal has strong volumetric expansion. As the coal is in the post-peak zone, fractures amalgamate to form channels for gas flow. It can greatly enhances the permeability and maintain the permeability at a high level. The maximum permeability (location a) is 2–3 orders higher than its initial permeability.
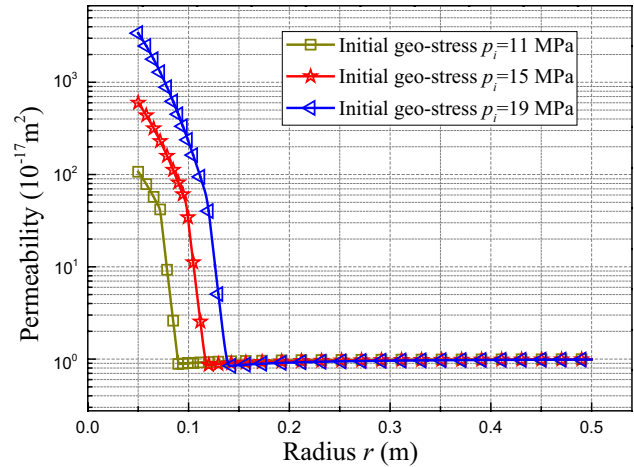

Fig. 11 Effect of initial geo-stress on permeability

Gas in this zone can flow freely from the high-pressure zone to the low-pressure zone. The gas pressure drops rapidly. This makes the pressure curve at $t = 1 \times 10^7$ s gentle and gas pressure gradient keeps small. Because of high permeability of coal, the zone I (a–b) is the full flow zone (FFZ) as described in Table 2. After that, the hoop stress σ_θ reaches its peak in the stress concentration area (b–c). The stress concentration compacts the coal and the permeability reaches its minimum. This higher vertical stress closes fractures and makes gas flow through this stress-increased zone more difficult. A pretty high pressure gradient is maintained in this zone. This poor permeability zone or II (b–c) forms a flow shielding (FSZ) as classified in Table 2. Beyond the location c, coal is in the elastic zone where the radial stress σ_r and the hoop stress σ_θ approach gradually to the initial stress state. The volumetric strain and permeability are steadily recovered to the
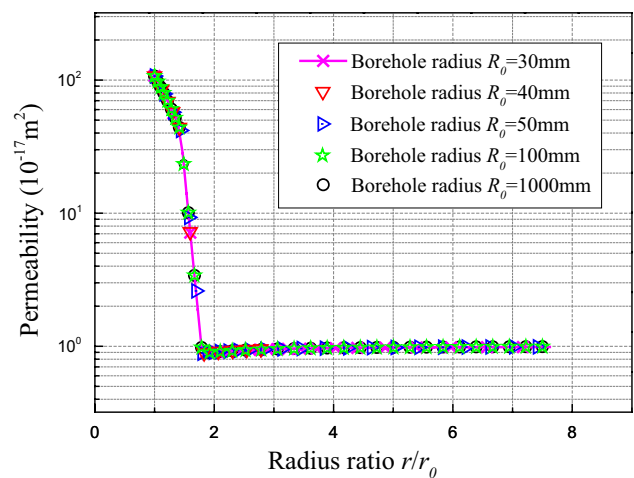

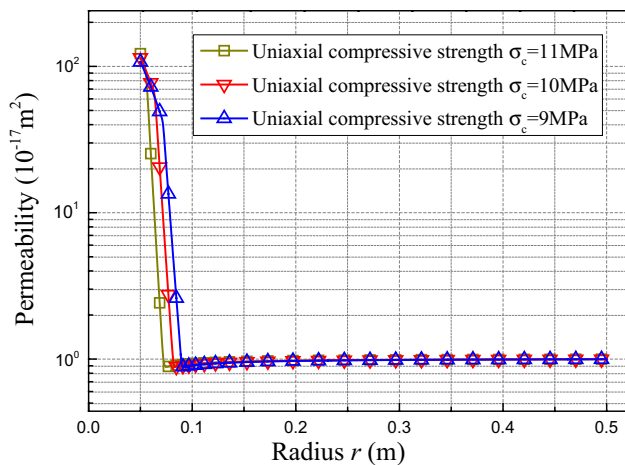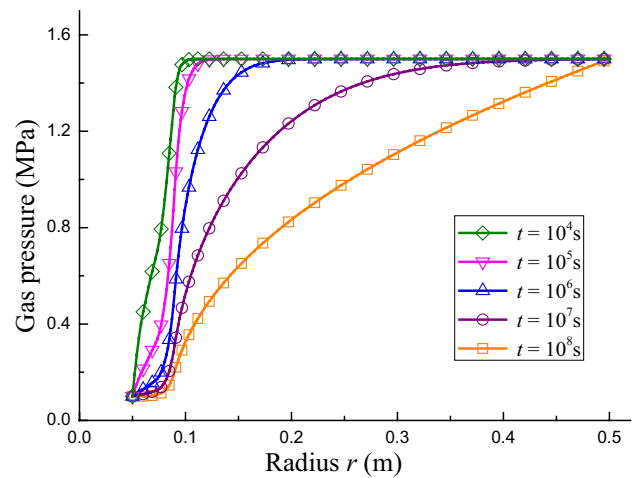**Fig. 12** Effect of excavation size on permeability

Fig. 13 Effect of uniaxial strength on permeability

(a) Gas pressure at different times (λ =4.5)

(b) Effect of damage enhanced coefficient at $t=1\times10^7$s

Fig. 14 Gas pressure distribution in coal mass around borehole

in situ state. The zone III (c–d) is the transitive flow zone (TFZ). At last, the coal enters into the zone IV (outside a–d), namely in situ rock flow zone (IRFZ), where the coal is not affected by drilling.
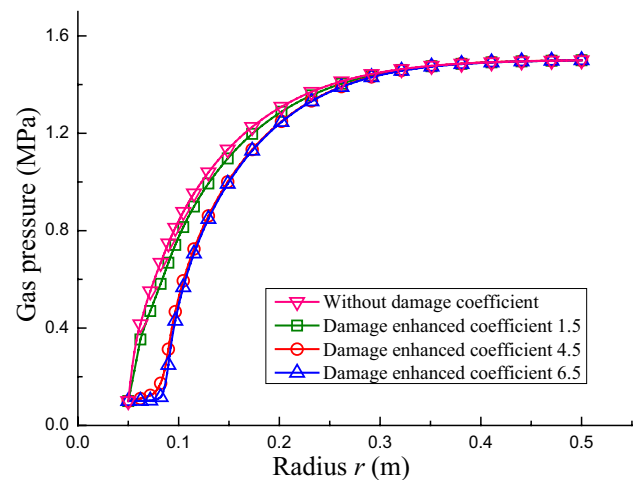
The dimension of the four zones can be roughly measured in this example. The full flow zone (FFZ) is nearby coal wall, about 30 mm long, the next is the flow-shielding zone (FSZ), about 20 mm long, then transitive flow zone (TFZ) follows, about 200 mm long, and finally the in situ rock flow zone (IRFZ). Due to stress release, the permeability is 2–3 orders of magnitude higher in the FFZ than in the IRFZ. However, the permeability in the FSZ is approximately 12% lower than that in the IRFZ due to stress concentration. The gas in the FSZ is difficult to flow, thus forming high pressure gradient zone. The permeability in the TFZ gradually increases from the small value in the FSZ to the initial value in the IRFZ. This demonstrated that the current compute approach is applicable to the formation analysis of gas accumulation. These results calculated by the approach can provide a theoretical guidance for gas drainage during the mining procedure.

Conclusions

In this study, analytical solutions of stress and strain and post-peak permeability model are combined to evaluate stress, strain, and permeability distribution of coal around a borehole, and gas flow equation is numerically solved to understand the distribution of gas pressure. Major findings can be drawn:

1. The approach proposed in this study is feasible to analyze the permeability distribution and gas pressure profile. This approach adopts the analytical solutions of stress and strain to describe deformation process and gas flow equation to describe the accumulation of gas content within coal seam. This approach has simpler computational procedure and higher computational efficiency.

2. Coal compaction in the elastic zone has important impacts on the distribution of permeability of a borehole and the accumulation of gas content. When m_e=0.8, the volumetric strain reaches its minimum of -0.05% and the permeability decreases gradually to the minimum of 8.86×10^{-18} m^2 at the radius of strain-softening zone. This compaction can make the permeability of coal in the elastic zone be smaller than the initial permeability.

Fig. 15 Distribution of stress, strain, permeability and gas pressure around borehole
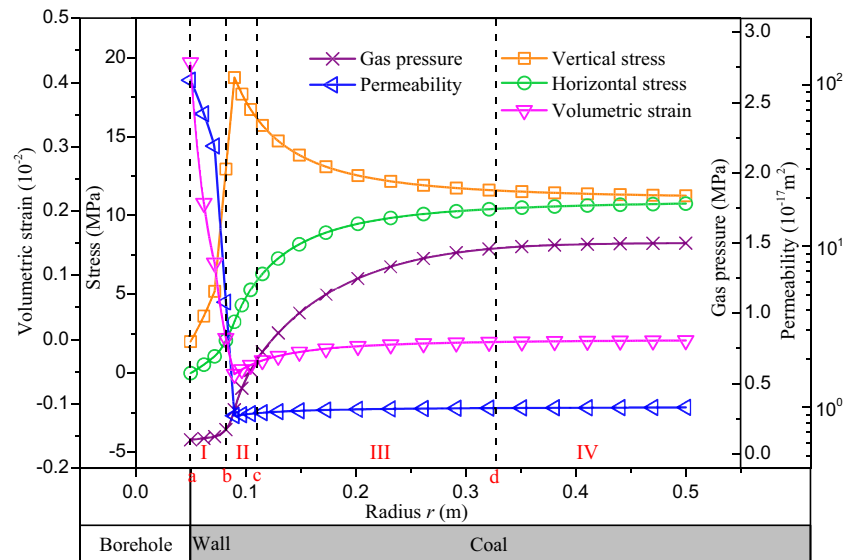
Table 2 Zone division of coal around a borehole

Zoning of stress–permeability–gas pressure curve	Divided by stress distribution	Divided by deformation	Divided by coal flow regime
I (a–b)	Post-peak failure	Residual + plastic	Full flow
II (b–c)	Stress concentration	Plastic + elastic	Flow shielding
III (c–d)	Pre-peak loading	Elastic	Transitive flow
IV (outside a–d)	In situ stress state	Elastic	In situ rock flow

This helps the coal seam form a flow-shielding zone near the interface between plastic zone and elastic zone.

3. The evolution of permeability is closely related to the physical properties of coal and the geological condition of coal seam. Higher initial geo-stress and lower failure strength have larger unloading zone and higher permeability enhancement. With the increase of drilling radius, both the residual state zone and the permeability enhancement zone are broadened while the permeability, hoop stress, radial stress and volumetric strain are only function of the normalized radius R/R_0.

4. The coal seam around a borehole can be divided into four zones based on their permeability distribution. Because of excavation-induced release of stress, the permeability in the FFZ was 2–3 orders of magnitude higher than the initial value. The permeability of the FSZ was lower than the initial value due to stress concentration, and gas in this zone is difficult to flow due to the stress concentration.

References

Adhikary DP, Guo H (2015) Modelling of longwall mining-induced strata permeability change. Rock Mech Rock Eng 48(1):345–359

Alonso E, Alejano LR, Varas F, Fdez-Manin G, Carranza-Torres C (2003) Ground response curves for rock masses exhibiting strain–softening behaviour. Int J Numer Anal Methods Geomech 27(13):1153–1185

Booth P, Brown H, Nemcik J, Ren T, Civil SO (2017) Spatial context in the calculation of gas emissions for underground coal mines. Int J Min Sci Technol 27(5):787–794

Borisenko AA (1985) Effect of gas pressure on stresses in coal strata. J Min Sci 21:88–92

Brown ET, Bray JW, Ladanyi B, Hoek E (1983) Ground response curves for rock tunnels. J Geotech Eng 109(1):15–39

Carranza-Torres C (2004) Elasto–plastic solution of tunnel problems using the generalized form of the Hoek–Brown failure criterion. Int J Rock Mech Min Sci 41:629–639

Chen HD, Cheng YP, Zhou HX, Li W (2013) Damage and permeability development in coal during unloading. Rock Mech Rock Eng 46(6):1377–1390

Chen D, Pan Z, Shi JQ, Si G, Ye Z, Zhang J (2016) A novel approach for modelling coal permeability during transition from elastic to post-failure state using a modified logistic growth function. Int J Coal Geol 163(1):132–139

Chu T, Jiang D, Minggao YU (2017) Experimental study of the seepage properties of the compacted particle coal under gradual loading. J China Univ Min Technol 46(5):1058–1065

Clarkson CR, Jordan CL, Geirhart RR, Seidle JP (2007) Production data analysis of CBM wells. In: SPE 107705, presented at the SPE rocky mountain oil and gas technology symposium, April 15–17, Denver

Cui X, Bustin RM (2005) Volumetric strain associated with methane desorption and its impact on coalbed gas production from deep coal seams. AAPG Bull 89(9):1181–1202

Gilman A, Beckie R (2000) Flow of coal–bed methane to a gallery. Transp Porous Media 41(1):1–16

Guan Z, Jiang Y, Tanabasi Y (2007) Ground reaction analyses in conventional tunnelling excavation. Tunn Undergr Space Technol 22(2):230–237

Hu QT, Zhang ST, Wen GC, Dai LC, Wang B (2015a) Coal–like material for coal and gas outburst simulation tests International. J Rock Mech Min Sci 74:151–156

Hu S, Zhou F, Liu Y, Xia T (2015b) Effective stress and permeability redistributions induced by successive roadway and borehole excavations. Rock Mech Rock Eng 48(1):319–332

Jin HW, Hu QT, Liu YB (2011) Failure mechanism of coal and gas outburst initiation. Proc Eng 26:1352–1360

Karacan C (2007) Development and application of reservoir models and artificial neural networks for optimizing ventilation air requirements in development mining of coal seams. Int J Coal Geol 72(3):221–239

Li CW, Fu S, Cui YG, Sun XY, Xie BJ, Yang W (2017) Study of the migration rule of high-concentration gas and spatial-temporal feature of gas hazard in the tunnel. J China Univ Min Technol 46(1):27–32

Lin BQ, Yang W, Wu HJ, Meng FW, Zhao YX, Zhai C (2010) A numeric analysis of the effects different factors have on slotted drilling. J China Univ Min Technol 39(2):153–157

Liu YB, Cao SG, Li Y, Wang J, Guo P, Xu J, Bai YJ (2010) Experimental study of swelling deformation effect of coal induced by gas adsorption. Chin J Rock Mech Eng 29(12):2485–2491

Liu Q, Cheng Y, Zhou H, Guo P, An F, Chen H (2015) A mathematical model of coupled gas flow and coal deformation with gas diffusion and Klinkenberg effects. Rock Mech Rock Eng 48(3):1163–1180

Liu T, Lin B, Yang W, Liu T, Zhai C (2017) An integrated technology for gas control and green mining in deep mines based on ultra-thin seam mining. Environ Earth Sci 76(6):243

Lu YE, Yang W (2013) Analytical solutions of stress and displacement in strain softening rock around a newly formed cavity. J Central South Univ 20:1397–1404

Men XX, Tang CA, Han ZH (2014) Numerical simulation on propagation mechanism of hydraulic fracture in fractured rockmass. Appl Mech Mater 488–489:417–420

Palmer I, Mansoori J (1996) How permeability depends on stress and pore pressure in coalbeds: a new model. In: 1996 SPE annual technical conference and exhibition society of petroleum engineers, Inc, Denver

Pan Z, Connell LD (2011) Modelling of anisotropic coal swelling and its impact on permeability behaviour for primary and enhanced coalbed methane recovery. Int J Coal Geol 85(3):257–267

Pan RK, Cheng YP, Yuan L, Yu MG, Dong J (2014) Effect of bedding structural diversity of coal on permeability evolution and gas disasters control with coal mining. Nat Hazards 73(2):1086–1092

Peng R, Ju Y, Wang JG, Xie H, Gao F, Mao L (2015) Energy dissipation and release during coal failure process in conventional triaxial compression. Rock Mech Rock Eng 48:509–526

Qu H, Liu J, Pan Z, Connell L (2014) Impact of matrix swelling area propagation on the evolution of coal permeability under coupled multiple processes. J Nat Gas Sci Eng 18:451–466

Saghafi A, Faiz M, Roberts D (2007) CO_2 storage and gas diffusivity properties of coals from Sydney Basin, Australia. Int J Coal Geol 70(1):240–254

Salmachi A, Karacan C (2017) Cross-formational flow of water into coalbed methane reservoirs: controls on relative permeability curve shape and production profile. Environ Earth Sci 76(5):200

Salmachi A, Yarmohammadtooski Z (2015) Production data analysis of coalbed methane wells to estimate the time required to reach to peak of gas production. Int J Coal Geol 141:33–41

Salmachi A, Sayyafzadeh M, Haghighi M (2013) Infill well placement optimization in coal bed methane reservoirs using genetic algorithm. Fuel 111(18):248–258

Salmachi A, Rajabi M, Reynolds P, Yarmohammadtooski Z, Wainman C (2016) The effect of magmatic intrusions on coalbed methane reservoir characteristics: a case study from the Hoskissons coalbed, Gunnedah Basin, Australia. Int J Coal Geol 165:278–289

Shi JQ, Durucan S (2004) Drawdown induced changes in permeability of coalbeds: a new interpretation of the reservoir response to primary recovery. Transp Porous Media 56(1):1–16

Singh AK, Singh R, Maiti J, Kumar R, Mandal PK (2011) Assessment of mining induced stress development over coal pillars during depillaring. Int J Rock Mech Min Sci 48:805–818

State Administration of Coal Mine Safety of China (2006) Cord for coal mine gas drainage China standard, Beijing

Tang CA, Tham LG, Lee PKK, Yang TH, Li LC (2002) Coupled analysis of flow, stress and damage (FSD) in rock failure. Int J Rock Mech Min Sci 39(4):477–489

Wang S, Elsworth D, Liu J (2013) Permeability evolution during progressive deformation of intact coal and implications for instability in underground coal seams. Int J Rock Mech Min Sci 58:34–45

Xue Y, Gao F, Gao Y, Cheng H, Liu Y, Hou P, Teng T (2016) Quantitative evaluation of stress-relief and permeability-increasing effects of overlying coal seams for coal mine methane drainage in Wulan coal mine. J Nat Gas Sci Eng 32:122–137

Xue Y, Gao F, Liu X, Liang X (2017) Permeability and pressure distribution characteristics of the roadway surrounding rock in the damaged zone of an excavation. Int J Min Sci Technol 27(2):211–219

Xue Y, Dang F, Shi F, Li R, Cao Z (2018) Evaluation of gas migration and rock damage characteristics for underground nuclear waste storage based on a coupled model. Sci Technol Nucl Installations 2018:2973279. https://doi.org/10.1155/2018/2973279

Yang XJ, Baleanu D (2013) Fractal heat conduction problem solved by local fractional variation iteration method. Therm Sci 17(2):625–628

Yang XL, Huang F (2010) Influences of strain softening and seepage on elastic and plastic solutions of circular openings in nonlinear rock masses. J Central South Univ Technol 17:621–627

Yarmohammadtooski Z, Salmachi A, White A, Rajabi M (2017) Fluid flow characteristics of Bandanna Coal Formation: a case study from the Fairview Field, eastern Australia. Aust J Earth Sci 64(3):319–333

Yin GZ, Jiang CB, Wang JG, Xu J (2013) Combined effect of stress, pore pressure and temperature on methane permeability in anthracite coal: an experimental study. Transp Porous Media 100(1):1–16

Yin GZ, Jiang CB, Wang JG, Xu J (2015) Geomechanical and flow properties of coal from loading axial stress and unloading confining pressure tests. Int J Rock Mech Min Sci 76:155–161

Yuan WB, Chen J (1986) Analysis of plastic zone and loose zone around opening in softening rock. J China Coal Soc 11(3):77–86

Zhang C, Wang J, Zhao J (2010) Unified solutions for stresses and displacements around circular tunnels using the unified Strength. Theory Sci China (Technological Sciences) 53(6):1694–1699

Zhu WC, Wei CH, Liu J, Xu T, Elsworth D (2013) Impact of gas adsorption induced coal matrix damage on the evolution of coal permeability. Rock Mech Rock Eng 46(6):1353–1366

Zhu WC, Gai D, Wei CH, Li SG (2016) High-pressure air blasting experiments on concrete and implications for enhanced coal gas drainage. J Nat Gas Sci Eng 36:1253–1263

Zhu W, Liu L, Liu J, Wei C, Peng Y (2018) Impact of gas adsorption-induced coal damage on the evolution of coal permeability. Int J Rock Mech Min Sci 101:89–97